Outbursting Quasi-Hilda Asteroid P/2010 H2 (Vales)

David Jewitt[1,2] and Yoonyoung Kim[3]

[1] Department of Earth, Planetary and Space Sciences, UCLA, 595 Charles Young Drive East, Los Angeles, CA 90095-1567, USA; jewitt@ucla.edu
[2] Department of Physics and Astronomy, University of California at Los Angeles, 430 Portola Plaza, Box 951547, Los Angeles, CA 90095-1547, USA
[3] Max Planck Institute for Solar System Research, Justus-von-Liebig-Weg 3, D-37077 Göttingen, Germany

Abstract

Quasi-Hilda asteroid P/2010 H2 (Vales) underwent a spectacular photometric outburst by $\geqslant 7.5$ mag (factor of $\geqslant 10^3$) in 2010. Here, we present our optical observations of this event in the four month period from April 20 to August 10. The outburst, starting UT 2010 April 15.70, released dust particles of total cross-section $17,600 \, \mathrm{km}^2$ (albedo 0.1 assumed) and mass $\sim 1.2 \times 10^9 \, \mathrm{kg}$, this being about 10^{-4} of the mass of the nucleus, taken as a sphere of radius 1.5 km and density $500 \, \mathrm{kg \, m^{-3}}$. While the rising phase of the outburst was very steep (brightness doubling time of hours), subsequent fading occurred slowly (fading timescales increasing from weeks to months), as large, low velocity particles drifted away from the nucleus. A simple model of the fading lightcurve indicates that the ejected particles occupied a broad range of sizes, from $\sim 1 \, \mu m$ to 6 cm, and followed a differential power-law distribution with index 3.6 ± 0.1 (similar to that in other comets). The fastest particles had speeds $\geqslant 210 \, \mathrm{m \, s^{-1}}$, indicating gas-drag acceleration of small grains well coupled to the flow. Low-energy processes known to drive mass loss in active asteroids, including rotational disruption; thermal and desiccation stress cracking; and electrostatic repulsion, cannot generate the high particles speeds measured in P/Vales, and are discounted. Impact origin is unlikely given the short dynamical lifetimes of the quasi-Hildas and the low collision probabilities of these objects. The specific energy of the ejecta is estimated at $220 \, \mathrm{J \, kg^{-1}}$. The outburst follows a series of encounters with Jupiter in the previous century, consistent with the delayed activation of buried supervolatiles (and/or the crystallization of subsurface amorphous ice) by conducted heat following an inward displacement of the perihelion. A potential origin in the debris cloud produced by avalanche is also considered.

Unified Astronomy Thesaurus concepts: Comets (280); Small solar system bodies (1469); Asteroids (72); Hilda group (741); Minor planets (1065); Short period comets (1452)

1. Introduction

Object P/2010 H2 (Vales) was discovered by Jan Vales as a $m_V \sim 12.5$ mag source in data taken with the 0.6 m telescope at Crni Vrh Observatory (Slovenia) on UT 2010 April 16.01 (Vales et al. 2010). While first noticed as a point source, visual observers began within a day to report an expanding coma (Mikuz et al. 2010; Vales et al. 2010). Prediscovery observations include an upper limit to the brightness $m_V \gtrsim 20$ on UT April 15.4 (Catalina Sky Survey observation by R. Kowalski, reported in Vales et al. 2010), another nondetection at unfiltered magnitude >16 on April 15.56 (Balanutsa et al. 2010) and a prediscovery detection at $m_V = 13.7 \pm 0.1$ on April 15.82 (Balanutsa et al. 2010), the latter two measurements with 0.4 m diameter telescopes of the MASTER network. Combined, the observations show sudden brightening of this previously unknown object with a doubling time of hours. Outbursts in comets are not rare (e.g., 13 were tabulated in a 9 yr period by Ishiguro et al. 2016), but few have amplitudes as large as the $\geqslant 7.5$ mag range (a factor of $\geqslant 10^3$) in P/Vales, and few have been observationally well-characterized, providing a motivation for this study.

The orbit has semimajor axis, $a = 3.850$ au, eccentricity, $e = 0.193$, and inclination, $i = 14°.3$, an orbital period of 7.56 yr and P/Vales passed perihelion (at 3.108 au) on UT 2010 March 9.3. The orbital elements give a Tisserand parameter with respect to Jupiter, $T_J = 2.99$, signifying strong gravitational interactions with that planet. This Tisserand is too small to qualify P/Vales as an active asteroid (Jewitt et al. 2015), for which $T_J \geqslant 3.08$ is a minimum requirement. P/Vales has instead been described as a Hilda asteroid (Hildas are bodies in orbit near the location of the 3:2 mean-motion resonance with Jupiter, at semimajor axis $a = 3.971$ au). P/Vales indeed lies within the orbital element range of the Hilda group as defined by Zellner et al. (1985), namely $3.7 \leqslant a \leqslant 4.2$ au, $e \leqslant 0.3$, and $i \leqslant 20°$. However, its semimajor axis is smaller than 96%, and its inclination larger than 92%, of the ~ 5000 objects in this semimajor axis range (Figure 1). Even though we refer to the osculating orbital elements (which change with time owing to perturbations from the planets), the figure serves to show that P/Vales is dynamically distinct from the typical Hilda asteroids clustered around the resonance. Supporting this difference, Marsden (2010) found that P/Vales passed within 1 au of Jupiter in 1976, and six comparably close encounters have occurred within the 20th century.[4] Consequently, we regard P/Vales as a likely "Quasi-Hilda," presumably a temporarily captured Jupiter-family comet, several examples of which have been previously described in the literature (e.g., Toth 2006; Gil-Hutton & García-Migani 2016).

The outburst of P/Vales attracted considerable observational attention over the spring and summer of 2010. We searched for additional detections of P/Vales from the prior and subsequent orbits in archival optical data, finding none. While some of the observations from 2010 were obtained by eye and are of limited scientific value, even calibrated observations taken with electronic detectors have failed to find their way into the

---

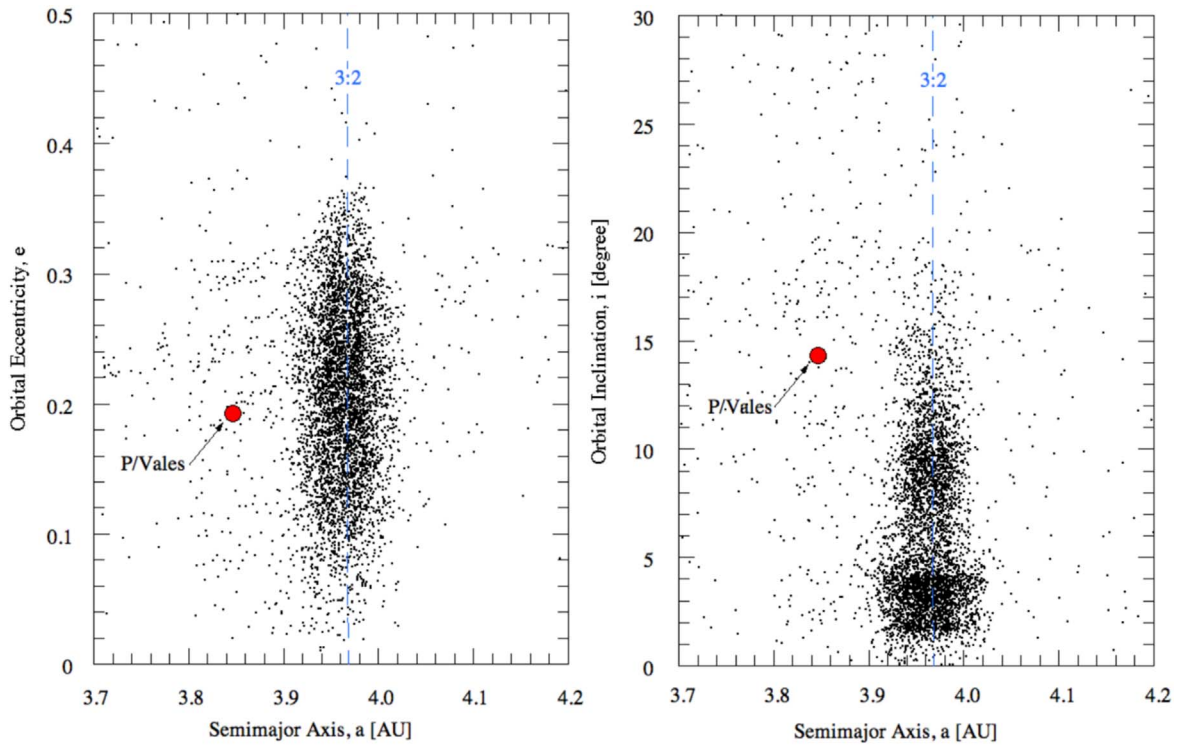[4] JPL Small Body Database Browser: https://tinyurl.com/y3kfyahe.

Figure 1. Left: semimajor axis vs. eccentricity for asteroids near the 3:2 mean-motion resonance with Jupiter (marked as a vertical dashed blue line). The location of P/2010 H2 (Vales) is marked with a red circle. Right: same as the left panel, but for semimajor axis vs. inclination. Obvious bimodal structure in the a vs. i plot reflects the existence of the Hilda and Schubart collisional families (Vinogradova 2015).

refereed literature, a situation we begin to reverse with this paper.

2. Observations

Early epoch observations were taken at our request only four days after the discovery, on UT 2010 April 20, using the "Baade" 6.5 m diameter Magellan telescope, located in Chile, by Scott Sheppard. We used a 2048×4096 pixel section of the IMACS short camera, giving a field of view approximately $400'' \times 800''$ at the $0''.2$ pixel^{-1} image scale. The seeing was $0''.7$–$0''.8$ FWHM. A total of 24 images of P/Vales were secured, with a range of exposure times from 2 to 300 s. After rejecting images in which the core of the target was saturated, we analyzed 3 images in Sloan g', 9 in Sloan r', and 4 in Sloan i'. Photometric calibration of the data was obtained using measurements of field stars, calibrated as part of the Deep Lensing Survey (Smith et al. 2002; Wittman et al. 2002).

Observations on UT 2010 June 6, 15, 18, and July 3 were obtained using the 0.9 m telescope of West Mountain Observatory, operated by Brigham Young University, in Utah. We used the Finger Lakes PL-09000 charge-coupled device, which gives a $25'.2$ field of view with $0''.49$ pixels. Images through a broadband Johnson-Cousins R filter were calibrated with reference to Landolt (1992) standard stars.

We also used the Keck 10 m diameter telescope atop Maunakea (altitude 4200 m) to observe P/Vales on UT 2010 August 20. The Low Resolution Imaging Spectrometer (Oke et al. 1995) possesses independent blue and red channels separated by a dichroic filter. We used the "460" dichroic (50% peak transmission at 4900 Å wavelength), and a broadband B filter on the blue side. The B filter has central wavelength $\lambda_C = 4370$ Å and FWHM $= 878$ Å. On the red side, we used a broadband R ($\lambda_C = 6417$ Å, FWHM $= 1185$ Å) filter. Photometric calibration of the data was secured using observations of standard stars selected to have Sun-like colors from the list by Landolt (1992) and cross-checked using field stars. Unfortunately, the seeing was unusually poor and variable, in the range $\sim 2''$–$3''$ FWHM. As a result, we present only large aperture photometry from Keck to assess the total magnitude of P/Vales.

A timeline of observations is given in Table 1 while representative composite images are shown in Figure 2.

2.1. Photometry

We elected to measure photometry within a nested set of circular apertures having projected, fixed radii of 5×10^3, 1×10^4, 2×10^4, and 4×10^4 km at the distance of P/Vales (Table 2). The use of fixed linear (as opposed to angular) apertures ensures that we measure the same volume around the nucleus independent of distance from the Earth, and obviates the need for a correction dependent on the surface brightness profile. Sky subtraction was determined from the median signal measured in a contiguous annulus with inner radius 4×10^4 km and extending out to $(1–2) \times 10^5$ km, depending on the data set. In some cases, we digitally removed background objects projected within the nested apertures. We obtained photometric calibration of the data using images of nearby Landolt (1992) standard stars and of field stars calibrated in the Pan-STARRS survey (Tonry et al. 2012; Magnier et al. 2013). Uncertainties on the photometry have several components. The values listed in Table 2 are the uncertainties determined empirically from the standard error on the mean of repeated measurements in each filter. Small, additional uncertainties arise from the differences in the bandpasses of the filters used at
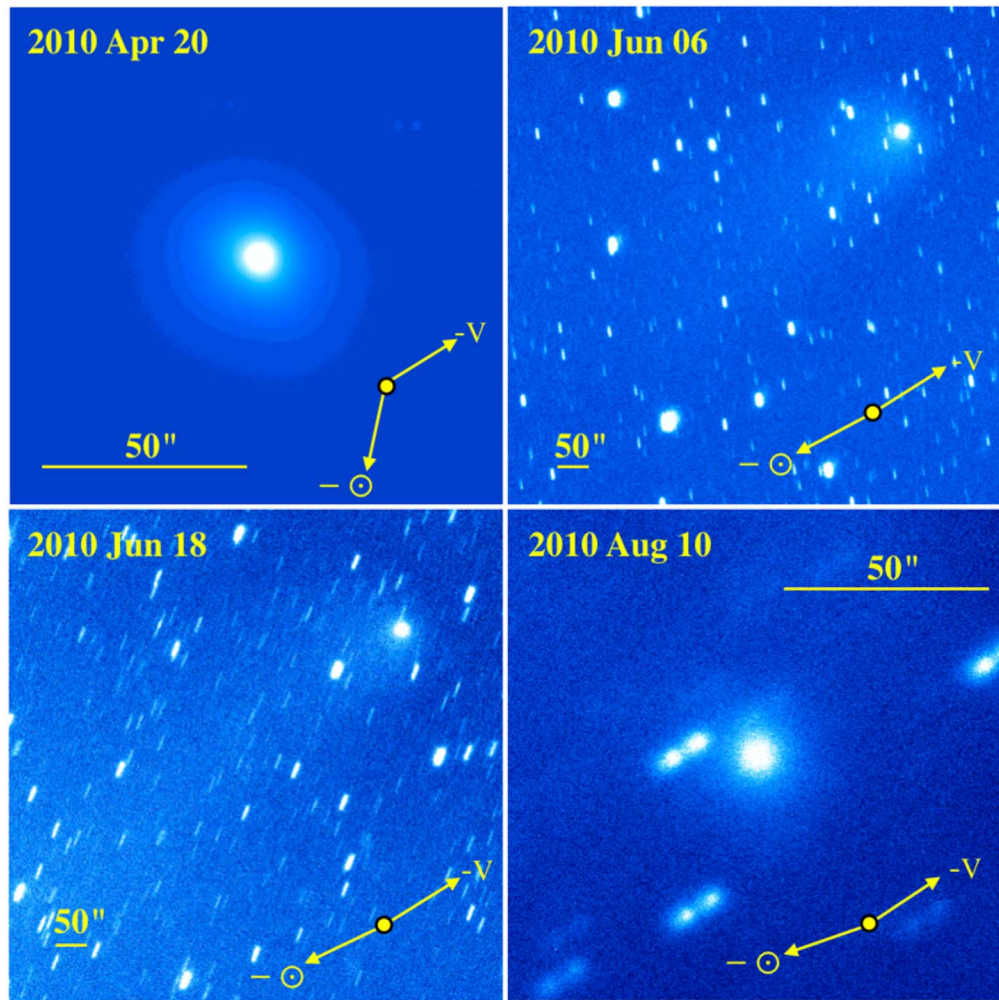
Figure 2. Images of P/Vales on four dates. Each panel has north to the top, east to the left, and is shown with a 50″ scale bar. The projected antisolar direction ($-\odot$) and the negative heliocentric velocity ($-V$) are shown as yellow arrows. The image from UT 2010 June 15 is indistinguishable from that on June 18, and so not shown. See Table 1 for additional observational details.

Table 1
P/Vales Timeline

UT Date	Event/Telescope[a]	DOY[b]	r_H[c]	Δ[d]	α[e]	ν[f]	$-\theta_\odot$[g]	$-\theta_V$[h]	$\delta_\oplus$[i]
2010 Mar 9.2	Perihelion	68.2	3.108	2.291	12.1	0.0	273.2	303.3	−6.0
2010 April 15.70	Outburst	105.7	3.112	2.131	4.6	7.3	186.2	302.2	−4.2
2010 Apr 20.2	Magellan 6.5 m	110.2	3.113	2.137	5.3	8.2	167.8	302.1	−3.8
2010 Jun 6.3	WMO 0.9 m	157.3	3.131	2.489	16.1	17.4	118.2	302.2	1.1
2010 Jun 15.3	WMO 0.9 m	166.3	3.136	2.598	17.4	19.1	112.9	302.4	1.8
2010 Jun 18.3	WMO 0.9 m	169.3	3.137	2.640	17.7	19.7	115.5	302.5	2.0
2010 Jul 3.2	WMO 0.9 m	184.2	3.147	2.840	18.7	22.6	113.1	302.9	3.0
2010 Aug 10.1	Keck 10 m	222.1	3.176	3.373	17.5	29.8	109.2	303.8	4.0

Notes.
[a] Event or telescope name and diameter.
[b] Day of Year, 1 = UT 2010 January 1.
[c] Heliocentric distance, in astronomical units.
[d] Geocentric distance, in astronomical units.
[e] Phase angle, degree.
[f] True Anomaly, degree.
[g] Position angle of the projected antisolar vector, degree.
[h] Position angle of the projected negative velocity vector, degree.
[i] Angle of the Earth above the orbital plane, degree.

Table 2
Fixed Aperture R-band Photometry[a]

UT Date	5000 km	10,000 km	20,000 km	40,000 km
2010 Apr 20.2	$13.09 \pm 0.02/8.87/4.3$	$12.35 \pm 0.01/8.13/8.4$	$11.86 \pm 0.01/7.64/13.2$	$11.55 \pm 0.01/7.33/17.6$
2010 Jun 06.3	$17.56 \pm 0.01/12.78/0.12$	$16.57 \pm 0.01/11.79/0.29$	$15.82 \pm 0.01/11.04/0.58$	$15.18 \pm 0.01/10.40/1.04$
2010 Jun 15.3	$18.04 \pm 0.02/13.14/0.08$	$16.97 \pm 0.01/12.07/0.22$	$16.16 \pm 0.01/11.26/0.47$	$15.52 \pm 0.01/10.62/0.85$
2010 Jun 18.3	$18.28 \pm 0.02/13.34/0.07$	$17.71 \pm 0.01/12.26/0.19$	$16.39 \pm 0.02/11.45/0.40$	$15.76 \pm 0.02/10.82/0.71$
2010 Jul 03.2	$18.67 \pm 0.03/13.54/0.06$	$17.57 \pm 0.02/12.44/0.16$	$16.66 \pm 0.01/11.53/0.37$	$15.99 \pm 0.01/10.86/0.68$
2010 Aug 10.1[b]	...	...	...	$17.08 \pm 0.03/11.58/0.35$

Notes.
[a] For each of four apertures of fixed projected radii 5×10^3 km, 10^4 km, 2×10^4, km, and 4×10^4 km, we list the apparent red magnitude, m_R, the absolute R magnitude, $m_R(1,1,0)$, and the scattering cross-section, C_e in units of 10^3 km^2 in the format $m_R/m_R(1,1,0)/C_e$.
[b] Inner apertures omitted owing to the influence of very poor seeing on this date.

Table 3
Measured Optical Colors[a]

Color	5000 km	10,000 km	20,000 km	40,000 km	Solar[b]
$B - V$	0.89 ± 0.02	0.90 ± 0.02	0.85 ± 0.02	0.74 ± 0.02	0.64 ± 0.02
$V - R$	0.51 ± 0.01	0.50 ± 0.01	0.50 ± 0.01	0.46 ± 0.01	0.35 ± 0.01
$R - I$	0.56 ± 0.01	0.55 ± 0.01	0.55 ± 0.01	0.51 ± 0.01	0.33 ± 0.01

Notes.
[a] Data from UT 2010 April 20.2.
[b] Solar colors from Holmberg et al. (2006).

each telescope and, particularly for the Landolt stars, intrinsic uncertainties of the magnitudes at the ± 0.01 to 0.02 mag level. These are all small compared with the uncertainty introduced by the unmeasured phase angle dependent darkening of P/Vales, and therefore of no consequence here. All photometry was converted to standard Kron-Cousins BVR magnitudes using transformation equations from Smith et al. (2002) for SDSS data and Tonry et al. (2012) where Pan-STARRS data were used.

We focus our analysis on the apparent R-filter magnitudes, m_R, which we convert into absolute magnitudes, $m_R(1, 1, 0)$, using

$$m_R(1, 1, 0) = m_R - 5\log_{10}(r_H \Delta) - \beta_{ph}\alpha. \quad (1)$$

Here, r_H and Δ are the instantaneous heliocentric and geocentric distances expressed in astronomical units, respectively, and α is the phase angle in degrees. Quantity β_{ph} is the phase coefficient, equal to the ratio of flux densities scattered at angle α to $\alpha = 0°$. The phase coefficient is unmeasured in P/Vales but studies of other comets show that in back-scattering (small α) geometries, $\beta_{ph} = 0.02$ mag degree^{-1} provides a useful approximation (Meech & Jewitt 1987).

The absolute magnitude provides a measure of the scattering cross-section, C (km^2), through

$$C = \frac{1.5 \times 10^6}{p} 10^{-0.4 m_R(1,1,0)}, \quad (2)$$

in which p is the geometric albedo. We assume $p = 0.1$ throughout, consistent with the nominal albedo of cometary dust (Zubko et al. 2017) and with the range of albedos (0.03–0.12) inferred in the possibly similar, outbursting comet 17P/Holmes (Ishiguro et al. 2010). The surfaces of Hildas have lower average albedos, $p \sim 0.05$ (Grav et al. 2012). As we note later, ice was reported in P/Vales (Yang & Sarid 2010), suggesting that a

higher albedo might be appropriate. On the other hand, ice becomes optically absorbing and dark unless very pure. In short, it is not obvious what the albedo of the ejected material should be, or even that albedo should be constant with respect to time since ejection. Cross-sections can be easily scaled to other albedos from Equation (2) by the factor $0.1/p$.

2.2. Color Photometry

Color measurements from UT 2010 April 20 are presented in Table 3, along with data for the colors of the Sun from Holmberg et al. (2006). All three independent color indices, $B - V$, $V - R$, and $R - I$, show evidence for a trend toward smaller values at larger radii, indicating that the outer parts of the coma are more blue than the inner parts (Figure 3). It is unlikely that the gradients are caused by gas contamination of the signal, both because the resonance fluorescence bands of common molecules are weak and rarely detected at 3 au and because these bands are largely confined to wavelengths $\lesssim 5000$ Å and would mainly affect $B - V$. All three color gradients gradients are individually significant at the 4σ level, and may be related to particle fragmentation inferred from the surface brightness profile (Section 2.3). However, we do not model this effect here, as color depends on many unknown properties of the dust (size, composition, and microstructure), any or all of which may vary with time in a transient body like P/Vales, and unique models of optical colors cannot be constructed. Instead, we use the colors for comparative purposes only.

The central colors are better representative of the source object and less likely to be affected by time-of-flight-dependent optical effects in small particles. Optically, the central (5000 km) colors of P/Vales are redder than the mean color of active short period comets ($B - R = 1.40 \pm 0.02$ versus 1.22 ± 0.02 for the comets; Jewitt 2015), but individual comets in the latter sample are scattered over the range $B - R = 1.0$ to 1.4, and some are as red as P/Vales. The colors of P/Vales are much redder than the colors of
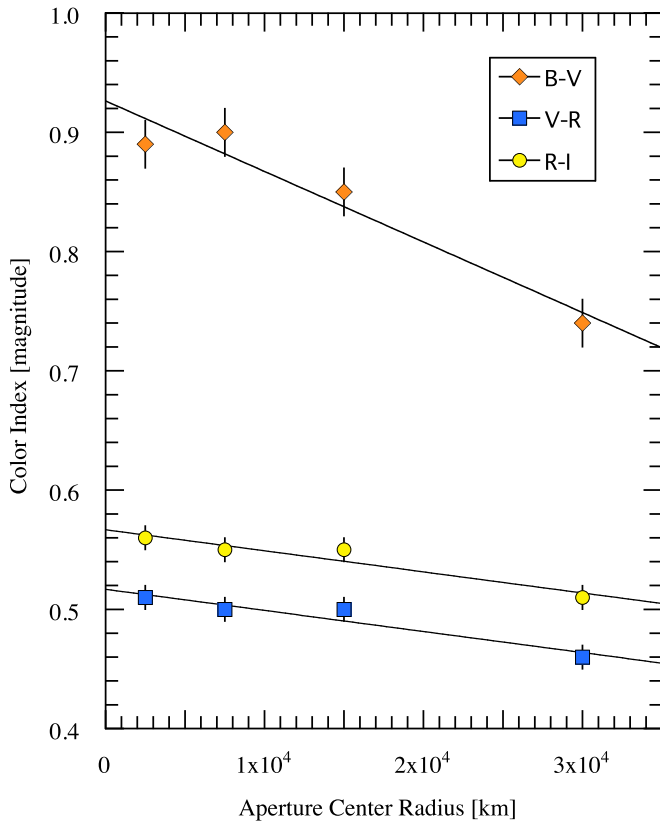
Figure 3. Color indices as a function of projected aperture radius from UT 2010 April 20.

Figure 4. Surface brightness profile of P/Vales on UT 2010 April 20 (yellow filled circles) and a field star (black filled circles). Interpolated lines have been added to guide the eye. In the upper right, line segments indicate logarithmic gradients $m = -1$ and $-3/2$, as marked.

inactive Hildas. For example, the spectral slope across the B to R region is about $S' = 20\%/1000\,\text{Å}$, whereas the slopes measured for Hildas are all $S' \leqslant 14\%/1000\,\text{Å}$ (Dahlgren & Lagerkvist 1995; Gil-Hutton & Brunini 2008). The red colors are more consistent with the mean colors of the nuclei of Jupiter-family comets (for which $B - V = 0.87 \pm 0.05$, $V - R = 0.50 \pm 0.03$, and $R - I = 0.46 \pm 0.03$; Jewitt 2015). This is not proof that P/Vales is a resonantly captured comet, but the colors are consistent with this interpretation. A single large aperture ($16\overset{''}{.}3$ radius, or 40,000 km) color measurement was obtained at Keck on UT 2010 August 10 under conditions of poor seeing, giving $B - R = 1.29 \pm 0.10$, consistent with the data from Table 3.

2.3. Surface Brightness Profile

We measured the surface brightness profile, $\Sigma(\theta)$, where θ is the angular distance from the nucleus, in the UT 2010 April 20 data as follows. The profile was computed using a nested set of concentric annuli each 1 pixel ($0\overset{''}{.}2$) wide, centered on the nucleus and with sky subtraction from a surrounding annulus having inner and outer radii 400 ($80''$) and 800 pixels ($160''$), respectively. The profile was extracted out to a radius of 100 pixels ($20''$). Similar measurements were taken to determine the point-spread function (PSF) from the profiles of field stars, using nearly simultaneous integrations of 10 s duration in which non-sidereal trailing is negligible. The profiles are shown in Figure 4.

As expected, the coma profile shows a central excess caused by the convolution of the comet profile with the PSF. At radius $\theta = 1''$, however, the coma surface brightness is already >10 times larger than the PSF brightness and, at larger radii, the effects of the convolution can be ignored. The profile becomes steeper at angular
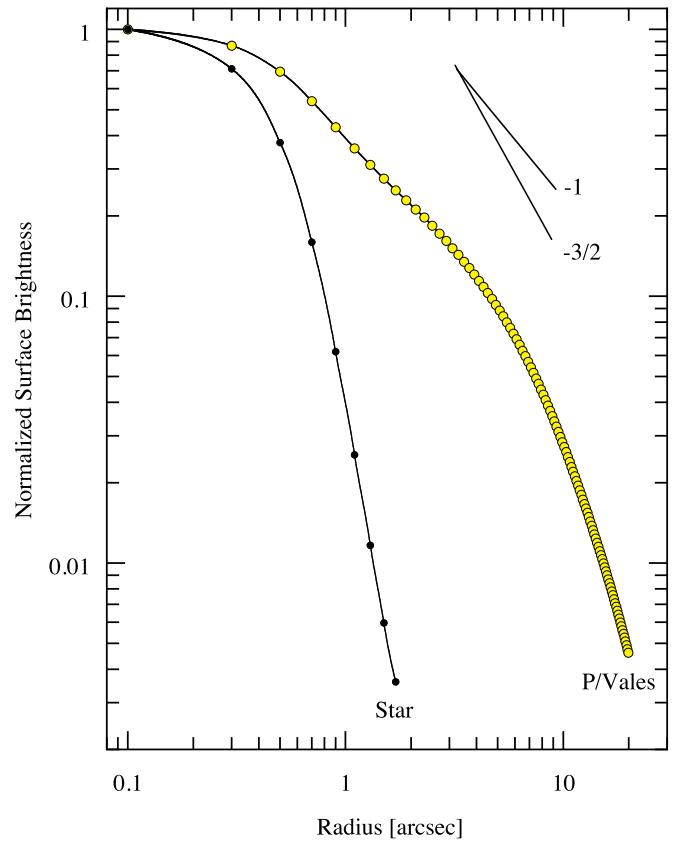
radii $\theta \gtrsim 4''$, as the physical edge of the coma is approached. The logarithmic gradient of the surface brightness is $m = d\ln \Sigma(\theta)/d\theta$. In the range $1'' \leqslant \theta \leqslant 4''$ (1545–6180 km at the comet), we find $m = -0.83 \pm 0.01$. The gradient is significantly less steep than the canonical $m = -1$ expected of a steady-state coma from the equation of continuity (Jewitt & Meech 1987). This could be because the coma is itself not in steady state, with production at the nucleus varying on a timescale comparable to or shorter than the residence time for dust particles. Alternatively, the shallow gradient could reflect fragmentation of ejected particles, resulting in the creation of extra scattering cross-section (and perhaps a change in broadband color) as distance from the nucleus increases. This was the case in 17P/Holmes, where an even flatter surface brightness profile, $m = -0.27$, was recorded (Stevenson & Jewitt 2012). The fractional increase in the cross-section varies as $\theta^{1+m} - 1$. With $\theta = 4''$ and $m = -0.83$, for example, the increase in the cross-section required to fit the gradient is by a modest $\sim 27\%$.

The spectroscopic detection of water ice in the comae of both 17P/Holmes (Yang et al. 2009) and P/Vales (Yang & Sarid 2010) suggests a role for sublimation. Specifically, composite grains bound together by water ice would spontaneously disaggregate through sublimation following their sudden expulsion from the nucleus into sunlight. The ice sublimation rate is a strong function of the grain temperature as set by the heliocentric distance and albedo. We solved the energy balance equation for an exposed, sublimating ice surface (see Section 4.1 of Jewitt et al. 2020). As an example, at $r_{\rm H} = 3.11$ au, we calculate that the sublimation rate from an isothermal water ice sphere of albedo 0.1 is $f_s = 2 \times 10^{-8}$ kg m^{-2} s^{-1}. The resulting sublimation lifetime of a grain of
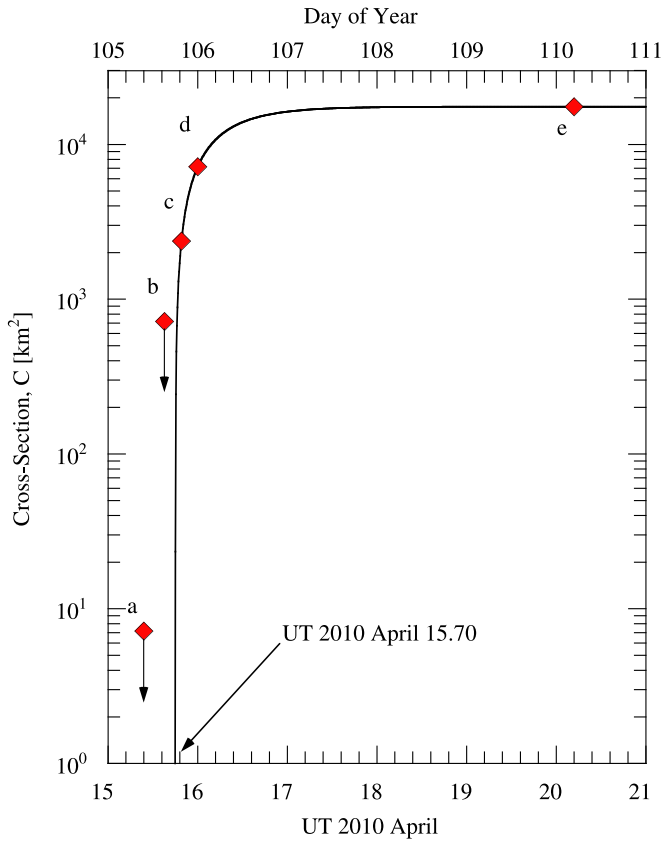
Figure 5. Early-time lightcurve showing nondetections (down-pointing arrows) from (a) Kowalski (reported in Vales et al. 2010) and (b) Balanutsa et al. (2010) at UT 2010 April 15.4 and 15.56, respectively. The first detection is (c) from April 15.82 (Balanutsa et al. 2010) and discovery is (d) at April 16.00 (Vales et al. 2010). Point (e) shows our first observation from April 20.2 (Table 1). The curve is an exponential fit to points (c), (d) and (e), indicating the start time UT 2010 April 15.70.

radius a is $t_s \sim a\rho/f_s$. By substitution, we estimate $t_s \sim 0.6$ to 6 days, for $a = 1$ to $10 \, \mu m$. As t_s is comparable to the ~ 4 days interval between the start of the outburst and the April 20 observation, we consider sublimation-induced disaggregation to be a plausible explanation of the shallow surface brightness gradient. Spatially and/or temporally resolved spectroscopic observations of ice absorption could test this explanation.

3. Discussion

3.1. Analytic Considerations

Nucleus radius, r_n. The strongest observational constraint on the nucleus radius is set by the nondetection at $m_V \geqslant 20$ from the Catalina Sky Survey on UT 2010 April 15.4, when $r_H = 3.112$, $\Delta = 2.131$, $\alpha = 4°.7$. By Equation (1) these values give absolute magnitude $m_V(1,1,0) \geqslant 15.8$ and, by Equation (2), a nucleus cross-section $C_n \leqslant 7.2 \, km^2$ and effective radius $r_n = (C_n/\pi)^{1/2} \leqslant 1.5 \, km$.

Start of outburst, T_0. The nondetections on UT 2010 April 15.4 (Vales et al. 2010) and 15.56 (Balanutsa et al. 2010) and the first detection on April 15.82 strongly bracket the beginning of the outburst. To obtain a better estimate of the start time within this range, we summarize the early-time observations in Figure 5, where we have converted the reported apparent magnitudes and limits to cross-sections, as described above. Upper limits to the cross-sections are marked in the figure with

down-pointing arrows. We fitted the three detections with an exponential function $C = C_0(1 - s \exp(-t/w))$, where $C_0 = 17,600 \, km^2$ is the peak cross-section determined on UT 2010 April 20.2 and s and w are constants. The function, plotted in the figure, extrapolates to $C = 0$ on UT 2010 April 15.70 (DOY 105.70) and provides our best estimate of the time of initiation. This is only 0.14 days (3 hours) after the nondetection reported by Balanutsa et al. (2010), 0.12 days (3 hours) before the first detection by the same observers, and 0.3 days (7 hours) before the discovery. Thus, even though the adoption of an exponential function is arbitrary, the data are highly constraining and there is little room for the start time to be much different from that indicated by the fit. The e-folding rise time of the cross-section given by the fit is $w^{-1} = 0.22$ days (5.4 hours), corresponding to a rise-time half-life $t_{1/2} = \ln(2)w^{-1} = 3.7$ hours. Even shorter rise-times (0.3–0.6 hours) were reported in early-phase observations of 17P/ Holmes (Hsieh et al. 2010). The peak measured cross-section, $C_{max} = 1.8 \times 10^4 \, km^2$ on UT 2010 April 20.2 (Table 2), is equal to that of a circle of radius $r \sim (C_{max}/\pi)^{1/2}$, or $r \sim 75 \, km$.

Particle parameters. The detailed appearance of the coma is influenced by the time-profile of the emission and by the distribution of particle radii. We take the latter to be a differential power law with index, q, such that the number of particles with radius between a and $a + da$ is $n(a) \, da = \Gamma a^{-q} da$ in the range $a_{min} \leqslant a \leqslant a_{max}$, with Γ equal to a constant. Before we apply a Monte Carlo approach to constrain the dust parameters, it is informative to use basic physics to assess the nature of the particles. We next obtain values for a_{min}, a_{max} and q to compare with values determined independently from a numerical model.

Lower size limit a_{min}. We make two morphological observations from the images taken on UT 2010 April 20.2. First, the coma extends in the sunward direction by a distance $\ell \sim 4 \times 10^7$ m. We interpret ℓ as the turnaround distance for dust particles ejected sunward at speed U, and subject to a constant radiation pressure induced acceleration. We write this acceleration as $\beta g_\odot$, where radiation pressure efficiency factor β is a dimensionless number and $g_\odot = GM_\odot/r_H^2$ is the local gravitational acceleration to the Sun. Parameter β is a function of particle size, shape, and composition. As a useful approximation for dielectric spheres, we take $\beta \sim 10^{-6}/a$, where a is the particle radius expressed in meters (Bohren & Huffman 1983). Then, the equation of motion for a fixed acceleration gives

$$\beta = \frac{2\ell r_H^2}{GM_\odot t^2}, \quad (3)$$

where $G = 6.67 \times 10^{-11}$ N kg^{-2} m^2 is the gravitational constant, $M_\odot = 2 \times 10^{30}$ kg is the mass of the Sun and t is the time of flight.

Second, the comet possesses no clear radiation-swept tail (i.e., dust particles launched sunward have been propelled to the antisolar side of the nucleus by a distance no greater than $-\ell$). Again, from the equation of motion for a fixed acceleration of $\beta g_\odot$, and substituting for β from Equation (3), we find

$$U = \frac{2\ell}{t}. \quad (4)$$

For the Magellan observation we set $t = 4.45$ days (3.8×10^5 s) and $\ell = 4 \times 10^7$ m to find $U = 210$ m s^{-1} and $\beta = 0.9$
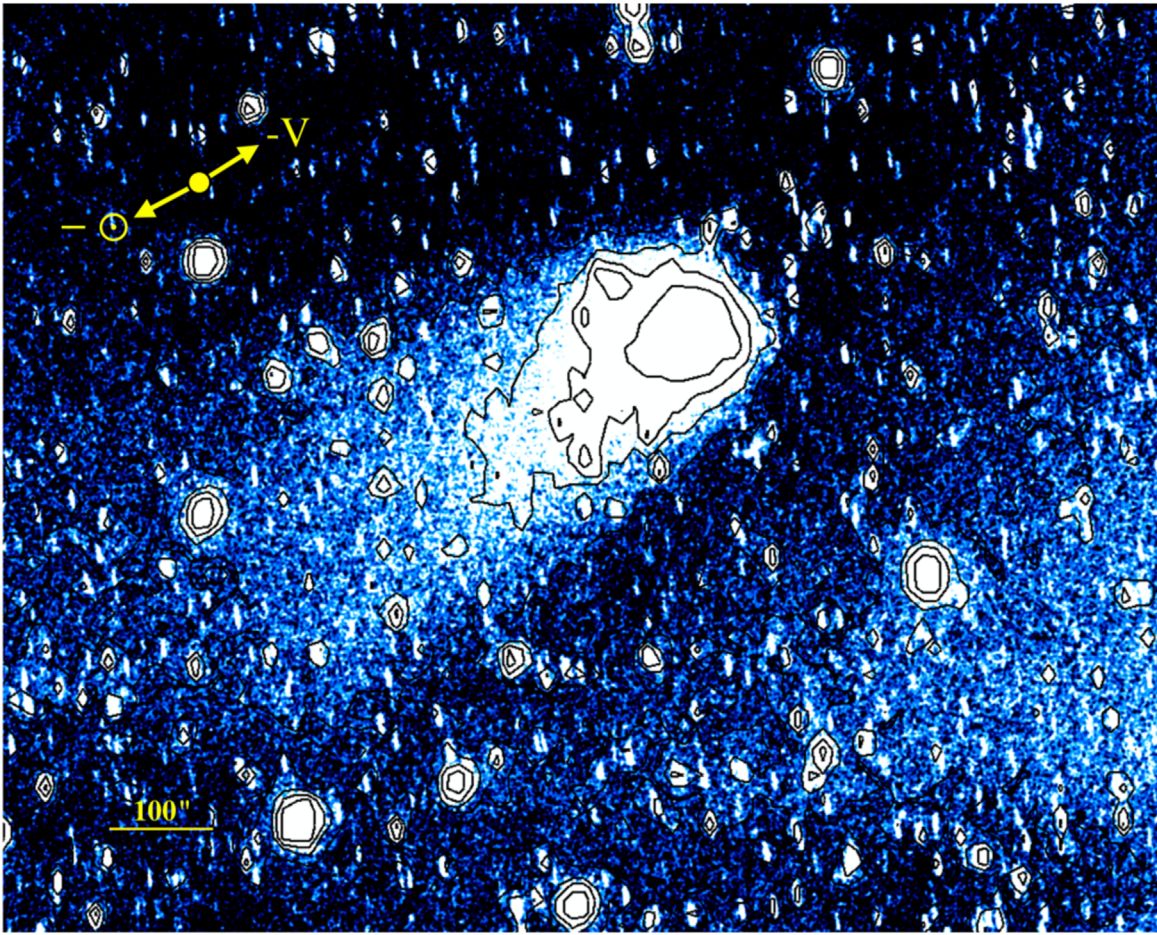
Figure 6. Hard stretch of P/Vales on UT 2010 June 6, with north to the top, east to the left, and a 100″ scale bar. The projected antisolar direction ($-\odot$) and the negative heliocentric velocity ($-V$) are shown as yellow arrows. The image has been smoothed by convolution with a Gaussian of 1″ FWHM to enhance faint structure. Light in the lower right is internally scattered from a bright field star. The tail extends to the edge of the image.

(implying $a \sim 1.1\ \mu$m). Strictly, ℓ is a lower limit to the true turnaround distance because of the effects of projection into the plane of the sky. Therefore, the derived values of U and β are also lower limits. For present purposes, however, these crude estimates are sufficient to show that the early-stage morphology of the envelope of the coma is controlled by fast-moving particles with radii $a \sim 1\ \mu$m.

By UT 2010 June 6 ($t = 52$ days after the outburst), the tail of P/Vales can be traced to the edge of the field of view, a distance $\ell \geqslant 1.3 \times 10^9$ m (Figure 6). Application of Equation (3) then gives $\beta \geqslant 0.3$ for the dust particles at the edge of the field of view. Again, the large-scale morphology on this date is controlled by the dynamics of micron-sized particles accelerated by solar radiation pressure. Large particles, less easily accelerated by radiation pressure, must be located closer to the nucleus on this date. The absence of a distinct feature attributable to large particles (specifically, a dust trail in data from UT 2010 June 6 (Figure 2), when the Earth was only $1°\!\!.1$ above the orbital plane of P/Vales (Table 1)), shows that the large particle contribution to the cross-section of the ejected material is minor on this date.

Upper size limit a_{max}. Larger particles are less well coupled to the outrushing gas and will have smaller terminal speeds. In gas-drag expulsion, the terminal speed of a dust grain is related to its radius by $U(a) = U_1 (a_0/a)^{1/2}$, where constant U_1 is the

speed of a particle at reference radius a_0. We take $a_0 = 10^{-6}$ m and $U_1 = 210$ m s^{-1}. To estimate the radius of the largest (slowest) particle that can be ejected against the gravity of the nucleus (ignoring possible effects of cohesion), we set $U = V_e$, where V_e is the gravitational escape speed, to find

$$a_{max} = \frac{3a_0 U_1^2}{8\pi G \rho r_n^2}, \qquad (5)$$

where we have assumed for simplicity that the nucleus is spherical and of density ρ. Substituting $r_n = 1.5$ km, we find from Equation (5) the largest ejectable dust radius, $a_{max} \sim 6$ cm. These large, low speed particles would take a time $t \sim 3 \times 10^7$ s (1 yr) to cross the 40,000 km photometry aperture, consistent with the persistence of excess cross-section in the lightcurve (Figure 7) on 100 days timescales.

Size-distribution index, q. Smaller, faster dust particles escape the photometry aperture more quickly than larger, slower ones. Therefore, in an impulsive outburst, the mean size of the particles in the aperture should increase with time because of the preferential loss of small particles, even as the total cross-section decreases. An expression for the fading caused by the selective loss of particles from a photometry aperture was derived by Jewitt et al. (2017). Here, we modify this expression to consider particles within an annulus, rather
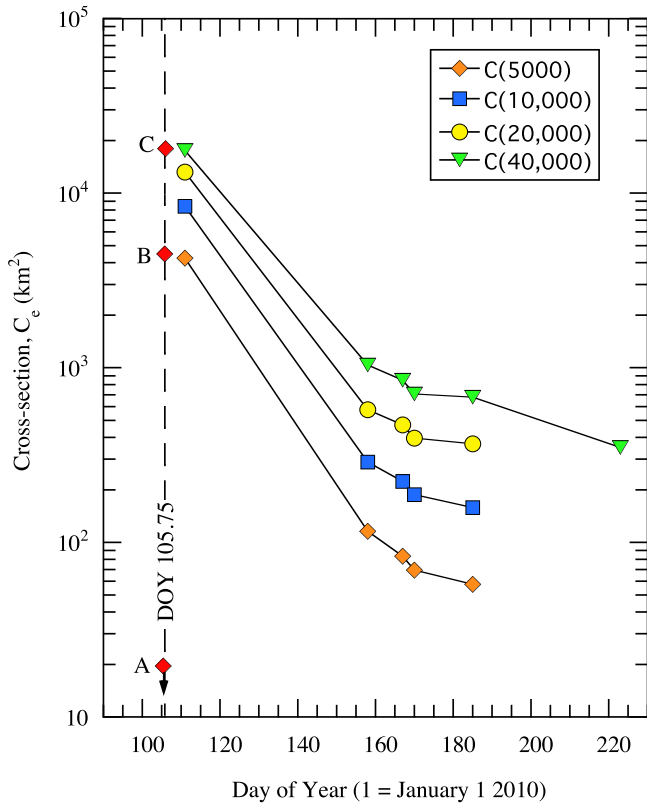
Figure 7. Scattering cross-section as a function of Day of Year in 2010. Red circles show A: an upper limit to the cross-section set by prediscovery data (reported in Vales et al. 2010), B: a prediscovery detection in the rise phase from Balanutsa et al. (2010), and C: the discovery (Vales et al. 2010). Other data from Table 2 Black lines connect data from each aperture. The date of outburst initiation is shown as a vertical dashed line.
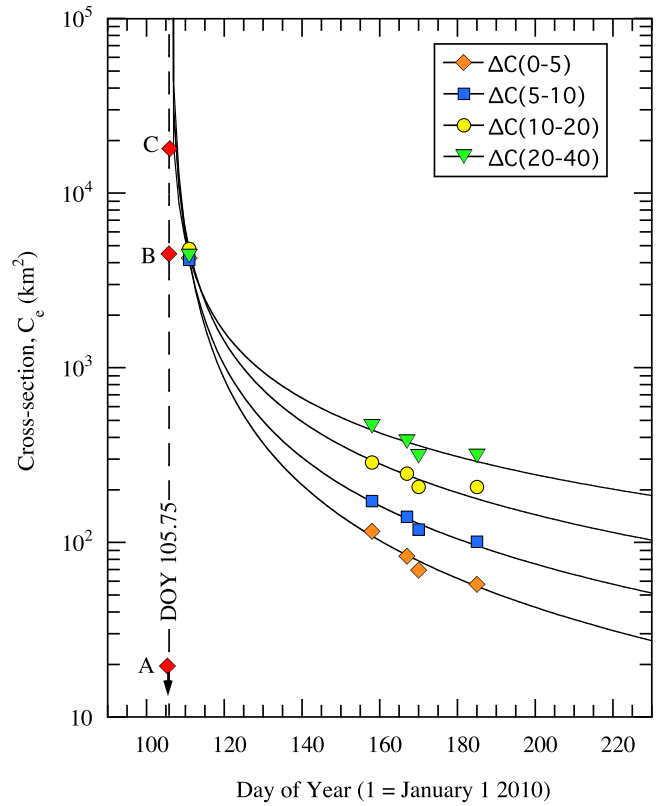

Figure 8. Annulus scattering cross-section vs. Day of Year. The black lines show least-squares fits to the data, yielding a particle size distribution index (differential) of $q = 3.58$, 3.64, 3.75, and 3.70, from top to bottom. Other features are the same as in Figure 7.

than a circular aperture, to compare with annular data extracted from Table 1.

Consider a photometry annulus with inner and outer radii, r_1 and r_2, respectively, and a measurement taken time t after the ejection. Particles traveling more slowly than $U_{\min} = r_1/t$ will not have reached the inner edge of the annulus, while those traveling faster than $U_{\max} = r_2/t$ will have escaped its outer edge. Substituting for the velocity–size relation, $U(a) = U_1(a_0/a)^{1/2}$, we find the critical radii

$$a_1(t) = a_0\left(\frac{U_1 t}{r_1}\right)^2 \text{ and } a_2(t) = a_0\left(\frac{U_1 t}{r_2}\right)^2. \quad (6)$$

Particles with radii $a < a_2(t)$ will have escaped the outer edge of the annulus after time of flight, t, while those with $a > a_1(t)$ travel so slowly that they have not yet reached the inner edge. Therefore, at any time, t, the particles within the annulus are confined to the radius range $a_2(t) < a < a_1(t)$, assuming impulsive emission.

The fraction of the ejected dust cross-section remaining within the annulus at time t as ejection is then

$$\frac{\Delta C(t)}{C(0)} = \frac{\int_{a_2}^{a_1} \pi a^2 n(a)\,da}{\int_{a_{\min}}^{a_{\max}} \pi a^2 n(a)\,da}, \quad (7)$$

where $C(0)$ is the total ejected cross-section. Substituting $n(a)da = \Gamma a^{-q} da$ and evaluating, we obtain

$$\frac{\Delta C(t)}{C(0)} = \left(\frac{a_0}{a_{\min}}\right)^{3-q}\left[\left(\frac{1}{r_1}\right)^{6-2q} - \left(\frac{1}{r_2}\right)^{6-2q}\right](U_1 t)^{6-2q}, \quad (8)$$

where we have assumed $a_{\max} \gg a_{\min}$, $q > 3$ and that the size range $a_1 - a_2$ is contained with $a_{\min} - a_{\max}$. The time dependence in Equation (8), $\Delta C(t)/C(0) \propto t^{6-2q}$, is the same as derived in Jewitt et al. (2017), and allows us to estimate q from the time-dependent annular photometry.

The four annular cross-sections, $\Delta C(t)$, are plotted in Figure 8. We least-squares fitted power laws to $\Delta C(t)$ to find the index, q from Equation (8). Lines in the figure show independent fits to photometry from the four apertures presented in Table 2. For the $\Delta C = $ 0–5000 km, 5000–10,000 km, 10,000–20,000 km, 20,000–40,000 km apertures we find, respectively, $q = 3.80$, 3.70, 3.61, and 3.50. The formal uncertainties on these fits are ± 0.01 to ± 0.02, but we use the standard error on the mean of the four values as a better measure of the true scatter. The mean size distribution index from fits to all four apertures is $q = 3.61 \pm 0.06$. Small differences between the values could result from many causes (perhaps the size distribution is not a power law, as assumed in Equation (8), perhaps the emission was not impulsive or the size-speed relation is invalid, perhaps the grain albedo changes with time as ice sublimates away). Given these many potential problems, the overall agreement between the four independent determinations of q is good. The derived value is close to $q = 3.7 \pm 0.1$ determined for fragmenting asteroid

P/2012 F5 (Gibbs) (Moreno et al. 2012) and $q = 3.6 \pm 0.6$ for fragmenting comet 332P/Ikeya–Murakami (Jewitt et al. 2016).

Dust mass, M. The mass of an optically thin collection of spheres is related to the sum of their cross-sections by

$$M = \frac{4}{3}\rho \bar{a} C, \qquad (9)$$

where $\bar{a}$ is the area-weighted mean particle size responsible for cross-section, C. The latter is given by

$$\bar{a} = \frac{\int_{a_{\min}}^{a_{\max}} a^3 \Gamma a^{-q} da}{\int_{a_{\min}}^{a_{\max}} a^2 \Gamma a^{-q} da}, \qquad (10)$$

which, for $q = 3.61$ simplifies to

$$\bar{a} = 1.56 a_{\max}^{0.39} a_{\min}^{0.61}. \qquad (11)$$

Substitution gives $\bar{a} = 1 \times 10^{-4}$ m (100 μm).

We see from Table 1 and Equations (9) and (11) that the peak dust cross-section, $C = 17.6 \times 10^3$ km^2, with $\rho = 500$ kg m^{-3}, gives dust mass $M = 1.2 \times 10^9$ kg. This is about 10^{-4} times the mass of the nucleus, considered as a sphere of the same density and radius 1.5 km. The bulk of this mass was released over a period $\tau \lesssim 1$ day (Figure 5), corresponding to a mean mass production rate $M/\tau \gtrsim 13{,}600$ kg s^{-1}. This rate is comparable to the (1 to 2) $\times 10^4$ kg s^{-1} measured in super-active comet C/1995 O1 (Hale–Bopp) at similar heliocentric distance (Weiler et al. 2003), although it is sustained in P/Vales for only a short period of time.

Specific energy, E/M. The energy per unit mass of ejecta is $E/M = (1/2)U^2(\bar{a})$. For a $q = 3.6$ distribution, the energy is carried by the small (fast) particles, because of the U^2 dependence, while the mass is carried by the large particles. With $\bar{a} = 100$ μm, $U(\bar{a}) = 21$ m s^{-1} and $E/M = 220$ J kg^{-1}. This specific energy is about 10^2 times smaller than the corresponding quantity estimated for comets 332P/Ikeya–Murakami and 17P/Holmes. The total energy of the outburst is $E \sim 3 \times 10^{11}$ J, an order of magnitude smaller than the outburst of 332P/Ikeya–Murakami and at least 10^3 times smaller than that of 17P/Holmes (summarized by Ishiguro et al. 2016).

3.2. Monte Carlo Model

We applied a 3D Monte Carlo simulation (Ishiguro et al. 2007) to P/Vales. In the model the motions of dust particles, under the action of solar gravity and radiation pressure, are followed as a function of particle size and time and direction of ejection. Our aim is not to reproduce the comet exactly since, given the number of free parameters in the model, a match can almost always be obtained. Instead, we aim to provide a consistency check of the results deduced analytically in Section 3.1.

As in Section 3.1, we set the dust velocity–size relation, $U(a) = U_1(a_0/a)^{1/2}$, as expected of gas-drag acceleration, with $U_1 = 210$ m s^{-1}. We further assumed the range of particle sizes $10^{-6} \leqslant a \leqslant 6 \times 10^{-2}$ m, a differential power-law index $q = 3.6$ and impulsive ejection on UT 2010 April 15.70. The model includes, as a free parameter, the angular dependence of the dust production rate, represented by a cone having its apex at the center of the nucleus, the Sun on its axis and a variable half-width, w. By experimentation, we found that w is most strongly constrained by the angular width of the dust tail in data

from 2010 June, and that there is a trade-off between w and U_1 in the dust speed versus size relation. Given the nominal speed $U_1 = 210$ m s^{-1}, we found that $w = 25°$ provided an acceptable fit to the tail. Values $w = 15°$ and $w = 35°$ produced tails, respectively, too narrow and too wide to fit the images from 2010 June.

Examples of the Monte Carlo simulations are shown in Figure 9, where it is seen that the parameters deduced analytically indeed generate models that match the data well. For example, the simulations show that, with the parameters deduced in Section 3.1, no large-particle trail can be discerned even near the crossing of the orbit plane on UT 2010 June 6 (Table 1). This is consistent with the absence of a trail in the data (Figure 9), confirming that large, slowly ejected grains present only a small fraction of the total cross-section even when spatially dispersed in the plane of the sky by radiation pressure. The simulations also reproduce the persistence of near-nucleus dust into 2010 August and the roughly circular late-stage appearance of the comet (Figure 9). This confirms that, by August 10, only the largest, slowest particles remain in the vicinity of the nucleus and the smaller particles, constituting the elongated tail in data from 2010 June, have been swept away. Overall, Monte Carlo simulations based on the parameters deduced in Section 3.1 provide an acceptable match to the broad-brush appearance of P/Vales.

Closer examination of the data shows evidence for unmodeled anisotropy in the coma in addition to that caused by solar radiation pressure. In Figure 10 we show, on the left, the image from UT 2010 April 20 and, on the right, the same image divided by a normalized profile in which the surface brightness varies inversely with angular distance from the nucleus (the location of which is marked in the figure by a black dot; Samarasinha & Larson 2014). The filtered image clearly shows excess emission near position angle 220°, and a broad deficit toward 330°. The amplitudes of these features are small (explaining why they are not evident in the left, unfiltered, image) but they confirm that mass loss from P/Vales was not isotropic. We have not attempted to model the anisotropy evident in Figure 10.

3.3. Outburst Mechanism

We briefly consider possible causes of the outburst of P/Vales.

The existence of high-speed ejecta, with $U \geqslant 210$ m s^{-1} for 1 μm particles, strongly suggests the action of gas drag. To see this, we note that, at $r_H = 3.112$ au, the local isothermal blackbody temperature is $T_{BB} = 158$ K while the mean thermal speed of H_2O molecules at this temperature is $V_{th} = (8kT_{BB}/(\pi \mu m_H))^{1/2}$, where $\mu = 18$ is the molecular weight of water and $m_H = 1.67 \times 10^{-27}$ kg is the mass of the hydrogen atom. We compute $V_{th} = 430$ m s^{-1}. The observation that, within a factor of two, $U \sim V_{th}$ for micron-sized dust grains is consistent with their acceleration by gas drag, as is the case in comets, generally.

Volatile explosion. Evidence for the interplay between cometary activity and dynamics is well-established. For example, the largest values of the non-gravitational accelerations of comets (which provide a measure of the mass loss rate) are correlated with recent, inward migration of the perihelion distance (Rickman et al. 1991). Could it be that the recent trapping of P/Vales into its quasi-Hilda orbit has triggered either enhanced sublimation of subsurface volatiles or the exothermic crystallization of buried amorphous ice, leading to
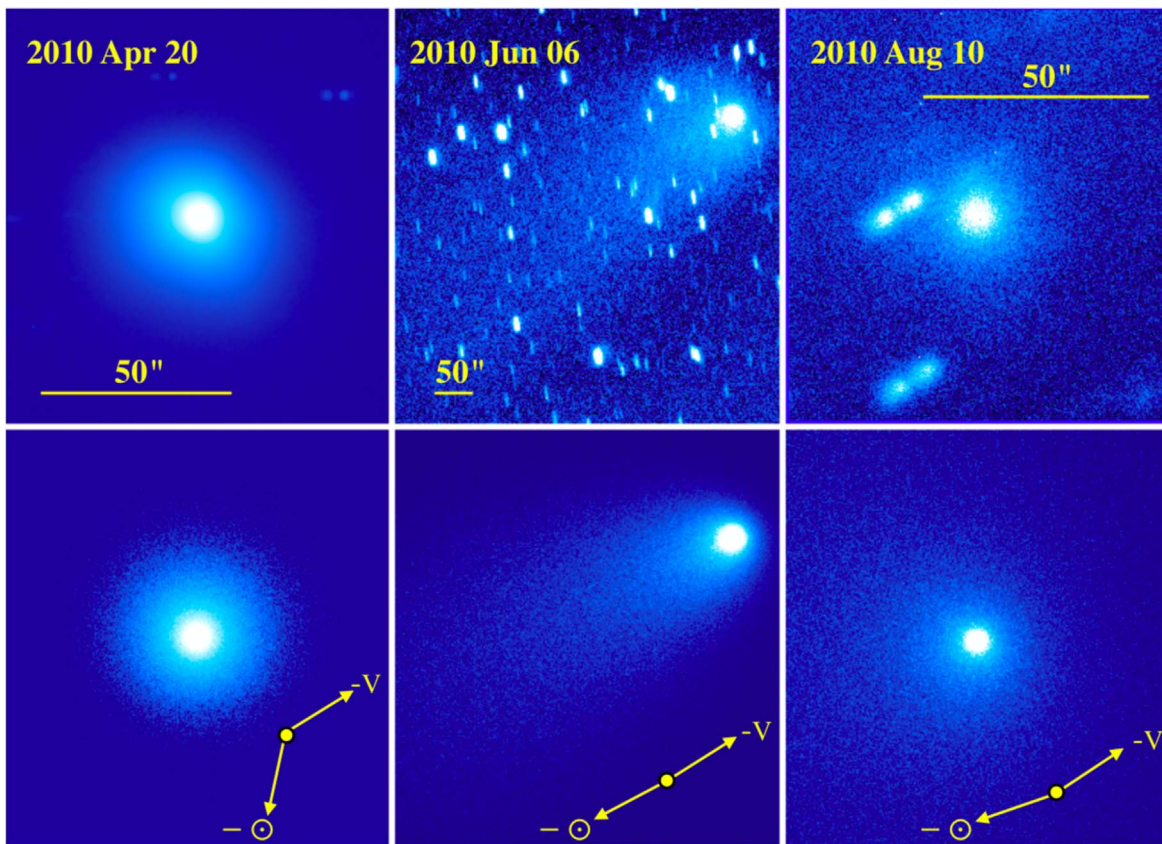
Figure 9. Monte Carlo simulations (bottom row) of P/Vales compared with images (top row) on three dates. Each panel has north to the top and east to the left, and scale bars and direction arrows as in Figure 2.
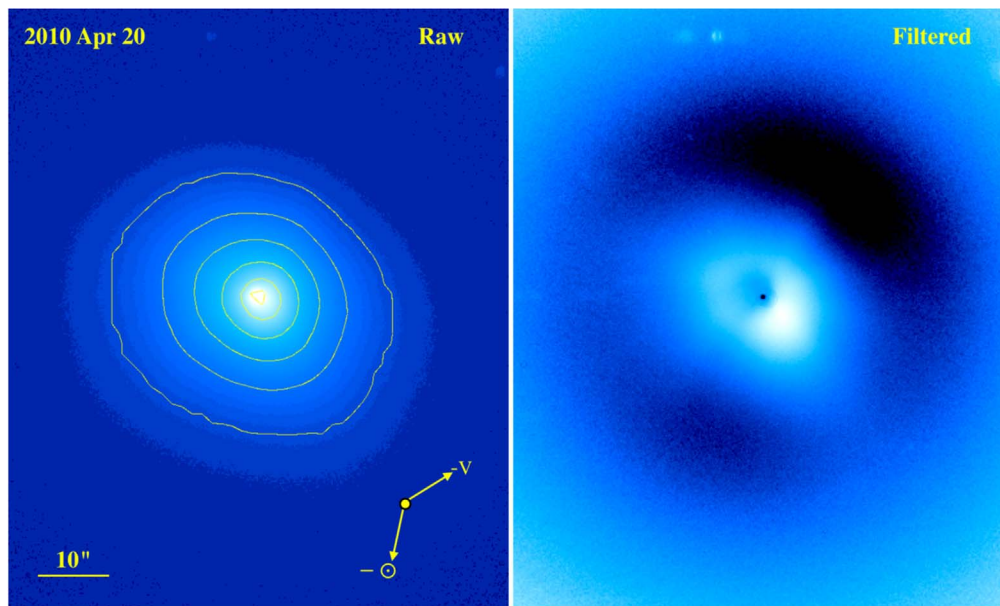

Figure 10. (Left) Image from UT 2010 April 20 (same as in the upper left panel of Figure 2) and (right) this image divided by a model in which surface brightness varies inversely with distance from the nucleus to suppress radial variations and enhance azimuthal ones. The enhanced panel, in which the location of the nucleus is marked by a black dot, clearly shows an excess of coma material to the southwest. In the left panel, the outermost contour is at 2.5 arbitrary units and successive contours are each brighter by a factor of two. A 10″ scale bar and direction arrows are shown. North is to the top, east is to the left.

pressure build-up and eventual rupture of a cohesive mantle (see Samarasinha 2001)?

In this scenario, the delay between the Jupiter encounters of the previous century and the outburst in 2010 would be a consequence of the slow conduction of heat from the surface to the buried ice. Solution of the conduction equation shows that the distance, d, over which heat is conducted in time τ is approximately $d \sim (\kappa\tau)^{1/2}$, where κ is the thermal diffusivity

of the material. The diffusivity of solid dielectric materials is $\kappa \sim 10^{-6}$ m^2 s^{-1}, but porosity reduces κ significantly. For example, laboratory measurements of highly porous dielectric powders give $\kappa \sim 10^{-9}$–10^{-8} m^2 s^{-1} (Sakatani et al. 2018). If we suppose that the most recent inward excursion of the perihelion distance occurred in 1973, the resulting $\tau = 35$ yr (10^9 s) delay would correspond to a buried ice depth $d \sim 1$–3 m. Earlier perihelion decreases would correspond to larger τ and deeper ice, but the diffusive $d \propto \tau^{1/2}$ dependence suggests that d is unlikely to be substantially larger than ~ 10 m.

The Monte Carlo models (Section 3.2) indicate ejection into a cone of half-angle $w \sim 25°$, amounting to a solid angle $\Omega \sim 0.2$ sr. Given this, we estimate the area of the region producing the outburst as $A_{\rm ice} = 4\pi r_n^2 (\Omega/4\pi)$ and the thickness of ice needed to provide the ejecta mass, M, as $d_{\rm ice} \sim M/(\rho\Omega r_n^2)$. Setting $M = 1.2 \times 10^9$ kg, $\rho = 500$ kg m^{-3} and $r_n \leqslant 1.5$ km, we find $A_{\rm ice} \leqslant 0.4$ km^2 (1.5% of the nucleus surface) and $d_{\rm ice} \geqslant 5$ m. Thus, a volatile pocket modest in both thickness and areal extent could supply the ejecta responsible for the outburst in P/Vales. The crystallization of amorphous water ice releases $\sim 10^5$ J kg^{-1}, far more than the average ~ 220 J kg^{-1} measured for the specific energy of the ejecta. Thus, even a very inefficient conversion of crystallization energy into kinetic energy would be sufficient to drive the outburst and we consider a delayed explosion caused by slowly conducted heat to be a plausible explanation for the outburst of P/Vales. On the other hand, whether amorphous ice could persist at meter depths in P/Vales depends on its past dynamical history which is, as with all comets, chaotic and unknown. We note that the spectrum reported by Yang & Sarid (2010) showed the 1.65 μm wavelength absorption indicative of water ice in the crystalline state. However, at the local blackbody temperature (158 K at 3.1 au), crystallization occurs in $\ll 1$ s, and the initial state of the ice before ejection into sunlight cannot be spectroscopically ascertained.

Cliff collapse. Could the outburst of P/Vales have resulted from the collapse of a cliff or an overhang on the nucleus surface? In this scenario, the collapsed material crumbles and spreads across the surface as a landslide from which the entrained volatiles sublimate, expelling dust and debris. A high-temperature Terrestrial analog might be found in the pyroclastic flows produced by gas-rich, high viscosity volcanic magmas, where ejected solids degas and move as a ground-hugging, dense flow. A cliff-collapse outburst of $\sim 10^6$ kg has been observed close-up on the nucleus of 67P/Churyumov–Gerasimenko (Pajola et al. 2017).

While qualitatively attractive, cliff collapse offers a less obvious explanation of the much larger ($\sim 10^9$ kg) outburst in P/Vales. To see this, we first note that the area $A_{\rm ice}$, estimated above, corresponds in this scenario to the area of the landslide needed to generate the outburst by sublimation. We solved the energy balance equation for sublimating carbon monoxide (CO) ice, considered as a representative supervolatile, finding that at $r_{\rm H} = 3.112$ au, the specific sublimation rate of a perfectly absorbing CO ice surface oriented normal to the Sun is $f_s({\rm CO}) = 4.6 \times 10^{-4}$ kg m^{-2} s^{-1}. The sublimation rate from the landslide is then just $dM/dt = f_s({\rm CO})A_{\rm ice}$. By substitution, $dM/dt \sim 180$ kg s^{-1}. This is an upper limit to the true dM/dt because the ice is unlikely to be perfectly absorbing (Pajola et al. 2017 determined an albedo ~ 0.4 in their example) and because the landslide surface is unlikely to be oriented perpendicular to the direction of the Sun. Significantly, dM/dt from this estimate is two

orders of magnitude smaller than the actual production rate obtained from the rising lightcurve, $M/\tau = 13,600$ kg s^{-1} (Section 3.1). Sublimation from a fresh landslide produced by cliff collapse cannot directly supply the massive outburst of P/Vales.

However, expulsion of ice-containing debris from the landslide surface into an expanding, avalanche-like cloud having cross-section $\gg A_{\rm ice}$ could strongly amplify the production rate. For example, we found that the peak measured cross-section is equal to that of a circle of radius $r \sim (C_{\rm max}/\pi)^{1/2}$, or $r \sim 75$ km (Section 3.1). Ice in these particles would then sublimate at a rate $\sim \pi r^2 f_s({\rm CO})$ which, with $r = 75$ km, could supply $dM/dt \sim 8 \times 10^6$ kg s^{-1}, two orders of magnitude larger than required by the data. Furthermore, if the cliff collapse were to expose amorphous ice, the resulting immediate exothermic crystallization could easily supply enough energy to drive the outburst. Particles with the mean radius $\bar{a} = 100$ μm have velocity $U \sim 20$ m s^{-1}, and would take ~ 1 hour to fill an optically thin hemisphere of radius 75 km, a timescale consistent with the short rise-time of the lightcurve (Figure 5). The coma was probably optically thin even at the time of the first detection (April 15.82, about 0.12 days after the best-fit initiation time on April 15.70, corresponding to a delay of ~ 3 hours). We conclude that cliff collapse of a sufficient volume could generate an outburst having the magnitude and the rapid rise-time implied by the observations.

An unresolved issue with the cliff-collapse hypothesis is one of timing. Why, other than by coincidence, would cliff collapse occur decades after the entrapment of P/Vales into the 3:2 mean-motion resonance? Perhaps low-level activity driven by the sublimation of near-surface water ice in the years prior to outburst caused incipient instability leading to collapse. In the absence of relevant observational evidence, however, we can say nothing about this possibility.

Impact. High-speed ejecta can also be produced by impact. However, two factors make an impact origin unlikely. First, the collision probability in the Hilda population ($P_i \sim 2 \times 10^{-18}$ km^{-2} yr^{-1}; Dahlgren 1998; Dell'Oro et al. 2001) is lower than in the main-asteroid belt ($P_i \sim 5 \times 10^{-18}$ km^{-2} yr^{-1}, Bottke & Greenberg 1993). The Hilda population is $\lesssim 1\%$ of the main-belt population and the quasi-Hilda population is orders of magnitude smaller still. Second, and more seriously, the quasi-Hildas have short dynamical lifetimes in the 3:2 resonance region (e.g., 10^3–10^4 yr, Gil-Hutton & García-Migani 2016). The likelihood of a substantial impact in this small population with a tiny residence window is very small. In the particular case of P/Vales, impact within a few decades, or even centuries, of its injection into the present orbit (Marsden 2010) is incredibly unlikely.

Other processes. The active asteroids are driven by several low-energy processes in addition to sublimation gas drag and impact (Jewitt 2012; Jewitt et al. 2015). These include rotational disruption of the parent body, cracking caused by thermal expansion and/or desiccation stresses, and electrostatic ejection of fine dust. None of these processes can offer a convincing explanation for the high speeds reached by the ejecta in P/Vales. In rotational disruption, for example, released material escapes with approximately the equatorial velocity of the rotation, typically $\leqslant 1$ m s^{-1} at breakup for a kilometer-sized body. Thermal fracture, with realistic efficiencies for conversion of strain energy into kinetic energy of ejected fragments in the 1%–10% range, produces peak speeds $\sim (1$–5) m s^{-1} (Equation (14) of Jewitt 2012). Electrostatic forces are weak, eject particles at similarly low speeds, and

cannot launch particles greater than micron-sized. The mismatch with the ejecta speeds measured in P/Vales effectively eliminates rotational disruption, thermal stresses, and electrostatics as relevant mechanisms.

4. Summary

We present time-resolved observations of the 2010 photometric outburst of P/2010 H2 (Vales). This is a quasi-Hilda object, probably emplaced near the 3:2 mean-motion resonance following a series of close encounters with Jupiter in the previous century.

1. The outburst, by $\Delta m_V \geqslant 7.5$ mag, started within a few hours of UT 2010 April 15.70, when 37 days past perihelion and at heliocentric distance 3.112 au.

2. Ejected particles had a maximum cross-section 17,600 km^2 and mass $\sim 1.2 \times 10^9$ kg (10^{-4} of the nucleus mass), with radii from microns to centimeters following a differential size distribution $n(a)da \propto a^{-3.61 \pm 0.06}$. Peak ejection rates were 13,600 kg s^{-1}, and the ejection appears to have been impulsive, with a timescale $\lesssim 1$ day.

3. High measured particle ejection speeds (up to 210 m s^{-1}) are compatible with gas-drag acceleration from sublimated ice. They are incompatible with rotational instability, thermal and desiccation stress fracture, and electrostatic repulsion, all of which are therefore ruled out as driving mechanisms. Asteroid impact, while capable of generating high-speed ejecta, is improbable given the small population and short dynamical lifetime of the quasi-Hildas.

4. P/Vales is most likely a temporarily captured comet in which conductive heating of subsurface ice has triggered an outburst, perhaps through exothermic crystallization from the amorphous state. If so, an ice volume about 0.4 km^2 in areal extent (about 1% of the nucleus surface) and $\geqslant 5$ m thick, and buried beneath a refractory layer a few meters thick, is inferred.

ORCID iDs

Yoonyoung Kim ● https://orcid.org/0000-0002-4676-2196

References

Balanutsa, P., Zimnukhov, D., Gorbovskoy, E., et al. 2010, ATel, 2578, 1
Bohren, C. F., & Huffman, D. R. 1983, Absorption and Scattering of Light by Small Particles (New York: Wiley)
Bottke, W. F., & Greenberg, R. 1993, GeoRL, 20, 879
Dahlgren, M. 1998, A&A, 336, 1056
Dahlgren, M., & Lagerkvist, C.-I. 1995, A&A, 302, 907
Dell'Oro, A., Marzari, F., Paolicchi, P., et al. 2001, A&A, 366, 1053
Gil-Hutton, R., & Brunini, A. 2008, Icar, 193, 567
Gil-Hutton, R., & García-Migani, E. 2016, A&A, 590, A111
Grav, T., Mainzer, A. K., Bauer, J., et al. 2012, ApJ, 744, 197
Holmberg, J., Flynn, C., & Portinari, L. 2006, MNRAS, 367, 449
Hsieh, H. H., Fitzsimmons, A., Joshi, Y., et al. 2010, MNRAS, 407, 1784
Ishiguro, M., Kuroda, D., Hanayama, H., et al. 2016, AJ, 152, 169
Ishiguro, M., Sarugaku, Y., Ueno, M., et al. 2007, Icar, 189, 169
Ishiguro, M., Watanabe, J., Sarugaku, Y., et al. 2010, ApJ, 714, 1324
Jewitt, D. 2012, AJ, 143, 66
Jewitt, D. 2015, AJ, 150, 201
Jewitt, D., Agarwal, J., Li, J., et al. 2017, AJ, 153, 223
Jewitt, D., Hsieh, H., & Agarwal, J. 2015, in Asteroids IV, ed. P. Michel, F. E. DeMeo, & W. F. Bottke (Tucson, AZ: Univ. Arizona Press), 221
Jewitt, D., Kim, Y., Mutchler, M., et al. 2020, ApJL, 896, L39
Jewitt, D., Mutchler, M., Weaver, H., et al. 2016, ApJL, 829, L8
Jewitt, D. C., & Meech, K. J. 1987, ApJ, 317, 992
Landolt, A. U. 1992, AJ, 104, 340
Magnier, E. A., Schlafly, E., Finkbeiner, D., et al. 2013, ApJS, 205, 20
Marsden, B. G. 2010, CBET, 2253
Meech, K. J., & Jewitt, D. C. 1987, A&A, 187, 585
Mikuz, H., Kowalski, R. A., Guido, E., et al. 2010, IAUC, 9137
Moreno, F., Licandro, J., & Cabrera-Lavers, A. 2012, ApJL, 761, L12
Oke, J. B., Cohen, J. G., Carr, M., et al. 1995, PASP, 107, 375
Pajola, M., Höfner, S., Vincent, J. B., et al. 2017, NatAs, 1, 0092
Rickman, H., Kamel, L., Froeschle, C., et al. 1991, AJ, 102, 1446
Sakatani, N., Ogawa, K., Arakawa, M., et al. 2018, Icar, 309, 13
Samarasinha, N. H. 2001, Icar, 154, 540
Samarasinha, N. H., & Larson, S. M. 2014, Icar, 239, 168
Smith, J. A., Tucker, D. L., Kent, S., et al. 2002, AJ, 123, 2121
Stevenson, R., & Jewitt, D. 2012, AJ, 144, 138
Tonry, J. L., Stubbs, C. W., Lykke, K. R., et al. 2012, ApJ, 750, 99
Toth, I. 2006, A&A, 448, 1191
Vales, J., Kowalski, R. A., Ryan, W., et al. 2010, CBET, 2249
Vinogradova, T. A. 2015, MNRAS, 454, 2436
Weiler, M., Rauer, H., Knollenberg, J., et al. 2003, A&A, 403, 313
Wittman, D. M., Tyson, J. A., Dell'Antonio, I. P., et al. 2002, Proc. SPIE, 4836, 73
Yang, B., Jewitt, D., & Bus, S. J. 2009, AJ, 137, 4538
Yang, B., & Sarid, G. 2010, BAAS, 42, 951
Zellner, B., Thirunagari, A., & Bender, D. 1985, Icar, 62, 505
Zubko, E., Videen, G., Shkuratov, Y., et al. 2017, JQSRT, 202, 104